Three dimensional characterization of nickel coarsening in solid oxide cells via ex-situ ptychographic nano-tomography

De Angelis, Salvatore; Jørgensen, Peter Stanley; Tsai, Esther Hsiao Rho; Holler, Mirko; Kreka, Kosova; Bowen, Jacob R.

Published in:
Journal of Power Sources

Link to article, DOI:
10.1016/j.jpowsour.2018.02.031

Publication date:
2018

Document Version
Peer reviewed version

Three Dimensional Characterization of Nickel Coarsening in Solid Oxide Cells via Ex-situ Ptychographic Nano-Tomography

Salvatore De Angelis[a], *Peter Stanley Jørgensen*[a], *Esther Hsiao Rho Tsai*[b] , *Mirko Holler*[b], *Kosova Kreka*[a], *and Jacob R. Bowen*[a]

a) Department of Energy Conversion and Storage, Technical University of Denmark

(DTU), Frederiksborgvej 4000, Denmark

S.D. Angelis: sdea@dtu.dk, P.S.Jørgensen: psjq@dtu.dk, K. Kreka: kkre@dtu.dk, J. R. Bowen: jrbo@dtu.dk

b) Paul Scherrer Institute (PSI),

5232 Villigen, Switzerland

E. H. R. Tsai: esther.tsai@psi.ch, M. Holler: mirko.holler@psi.ch

Corresponding author:

Jacob Ross Bowen

Department of Energy Conversion and Storage, Technical University of Denmark

(DTU), Frederiksborgvej 4000, Denmark

Email: jrbo@dtu.dk

Abstract

Nickel coarsening is considered a significant cause of solid oxide cell (SOC) performance degradation. Therefore, understanding the morphological changes in the nickel-yttria stabilized zirconia (Ni-YSZ) fuel electrode is crucial for the wide spread usage of SOC technology. This paper reports a study of the initial 3D microstructure evolution of a SOC analyzed in the pristine state and after 3 and 8 hours of annealing at 850 °C, in dry hydrogen. The analysis of the evolution of the same location of the electrode shows a substantial change of the nickel and pore network during the first 3 hours of treatment, while only negligible changes are observed after 8 hours. The nickel coarsening results in loss of connectivity in the nickel network, reduced nickel specific surface area and decreased total triple phase boundary density. For the condition of this experiment, nickel coarsening is shown to be predominantly curvature driven, and changes in the electrode microstructure parameters are discussed in terms of local microstructural evolution.

Introduction

Solid oxide fuel cells (SOFC) and electrolysis cells (SOEC) are electrochemical devices able to efficiently convert chemical energy to electrical energy and vice-versa. When connected to renewable energy sources such as solar panels or wind turbines, hydrogen can be produced from water electrolysis to be used in electricity production in cases of high energy demand or in absence of sufficient light or wind[1–3]. For solid oxide cells, in order to represent a cost-effective and efficient storage technology, long-term durability under harsh operating conditions is crucial [4]. To date, state-of-the-art SOC fuel electrodes consist of a porous composite cermet of nickel and yttria-stabilized zirconia (YSZ). While nickel is an excellent electron conductor and exhibits high catalytic performance at high temperature, it undergoes severe microstructural changes during operation, which leads to degradation of the cell performance.

Due to the nickel high specific surface area, the system is expected to minimize its free energy through curvature minimization and particle agglomeration [5,6]. Furthermore, the low wettability between Ni and YSZ also contributes to the driving forces [7]for Ni network coarsening [8,9]. In previous reports, Ni coarsening has

been studied by electrochemical impedance spectroscopy (EIS)[10,11], SEM analysis [12] and more recently through FIB-SEM [13,14] and X-ray nano-tomography [15,16]. *Kennouche et al.* analyzed different samples after aging at different temperatures and time[15] and concluded that, at 900 °C, there is a rapid evolution of the nickel and the pore phases during the early stages of annealing. However, in most of the previous reports[15,16], different samples were analyzed *post-mortem* after aging and then compared with reference specimens. Following this approach, only global statistical parameters such as triple phase boundary length, surface areas and particle size distribution can be used in the comparison. Presently it is unknown if initial coarsening mechanisms are different to those operating at longer time scales. However, the rapid evolution observed in the very early stages of ageing/annealing[15], warrants investigate the coarsening phenomena after shorter periods of time and at higher time resolution.

Theoretical studies on the Ni coarsening have been performed using a variety of techniques ranging from simple coarsening models[17] to cellar automaton[18] and 3D phase-field simulations[7,19–21]. Using the phase-field approach, *Chen et al.* simulated the Ni coarsening in a real Ni-YSZ microstructure considering the wetting angle between Ni and YSZ[15], while *Jiao and Shikazono* included also crystallographic information[22]. While both studies used experimental reconstructed microstructure as starting geometry for the phase-field model, only the evolution of statistical parameters (TPB length, surface area etc.) could be used in the comparison between experimental data and simulation results.

Kennouche et al. realized the first *ex-situ* Ni-YSZ annealing experiment where the same sample was successfully analyzed in its pristine state and after 24 and 48 hours of heat treatment at 1050 °C in 5% H_2/3% H_2O/95% Ar [23]. This pioneering work shows that, at high annealing temperature, it is possible to achieve significant structural evolution on the time scale of a synchrotron beam time.

The present work capitalizes on high-quality multi-keV pytchographic X-ray 3D imaging [24,25] with the aim to investigate the details of nickel microstructure evolution with high spatial resolution during the early stages of coarsening, at temperatures representative of Ni-YSZ electrode operation.

2. **Experimental methods**

2.1 ***Sample preparation***

The ideal sample for a measurement using ptychographic x-ray computed tomography (PXCT)[26] has a cylindrical cross section, small enough to minimize the measurement time (reduced scanning field of view) and avoid excessive absorption in dense samples. In the traditional lift-out technique for nano-tomography experiments, the specimen is cut out of the bulk sample and it is subsequently mounted on a suitable sample holder using platinum micro-welding [27]. This procedure is performed inside a focused ion beam scanning electron microscope (FIB-SEM) with the help of a micro manipulator. However, it has been observed that the Pt welding is unstable at SOC operation temperatures, resulting in macroscopic movement of the sample after the thermal treatment [28]. Samples are required to be sufficiently large to secure rigid attachment to the sample holder whilst, at the same time, contain a region with a small cylindrical but microstructurally representative cross section for meeting the aforementioned nano-tomography requirements.

Following a similar procedure reported in our previous work [25], the sample was prepared from a typical Ni-YSZ (Yittria-Stabilized-Zirconia) anode supported SOFC half-cell. The starting NiO-YSZ cermet was reduced for 1 h at 850 °C in a mixture of 9% H_2 in N_2. Details of the cell production can be found elsewhere [29]. The cell presents a functional layer (Ni-8YSZ mol. 8% Y_2O_3) of ~15 µm. From the reduced half-cell, a ~3 mm long and 300 µm wide slice was carefully cut using a diamond cutting wheel (Minitom, *Struers*). The slice was precision polished (MultiPrep, Allied High Tech Products, Inc) at an angle to form a truncated asymmetric pyramidal sample of 60x60 µm at the top. A standard cSAXS sample holder was modified in order to accommodate the sample in its center of rotation and minimize sample tilting. The specimen was temporally mounted on the holder using super glue (Loctite 460, *Loctite Corp.,* ONT) prior to being securely attached with platinum paste (CN38-019B Platinum Conductive Paste, *Ferro*). The entire procedure was carried out manually under an optical microscope to be within 100 µm from the beamline stage rotation axis. The super glue allows enough flexibility for fine adjustment of the sample position on the holder. Once the sample is centered, platinum paste is used to secure the latter for high temperature treatment. FIB milling (CrossBeam X1540, *Zeiss*) was used to produce a cylindrical pillar, ~14 µm in diameter and ~15 µm in height using a 10 nA probe current ion beam.

2.2 Tomography procedure

The PXCT experiment was performed at the X12SA (cSAXS) beamline at the Swiss Light Source, Paul Scherrer Institut, Switzerland using the instrumentation describped in[30]. The ptychographic procedure was carried out at 7.2 keV with a scanning field of view of 19 x 11 µm. At each scanning point, a diffraction pattern[31] was recorded 7.4 m downstream of the object using a Pilatus 2M detector[32] with 172×172 µm^2 pixel size at 0.1 s exposure time. Diffraction patterns with sizes of 400×400 pixels were used in the ptychographic reconstruction, giving an object pixel size of 18.4 nm. For each dataset, 500 projections over an angular range of 180° were collected. Three-dimensional ptychographic tomograms were obtained through fine alignment of the reconstructed 2D projections and filtered back projection[33,34]. Ptychography allows quantitative 3D images of the electron density of the sample[35]. Subsequently, the electron density can be converted to mass density if the chemical composition is known and the measurements are taken away from the absorption edges of the constituent materials [24]. For this dataset, a resolution of 55 nm has been computed using the Fourier Shell Correlation method [24].

The sample was initially imaged in the pristine state (right after the reduction of the starting NiO-YSZ cermet) and then subsequently after additional annealing steps of 3 and 5 hours at 850 °C in a gas mixture of 4% H_2 and 96% N_2 for a total of 8 hours of exposure at maximum temperature. The treatments were conducted in a small custom-made tube furnace with a flow rate of 5 l/h. The ramping rate for each treatment was 10°C /min for both heating and cooling (see Figure S1 in the supplementary materials).

2.3 **Segmentation, registration and microstructural quantification**

The pristine dataset was first rotated in order to orient the electrolyte parallel to the x axis. The remaining 2 volumes were then registered to the pristine dataset. A coarse transformation was determined manually followed by a 3D rigid transformation computed by the iterative closest point method [36]. In the calculation, only points sampled from the stable YSZ phase were used. The raw volumes (the pristine dataset is available here DOI: 10.5281/zenodo.1040274) were segmented using a 2D (intensity vs. intensity gradient magnitude) histogram thresholding procedure. Microstructural quantitative characterization of particle sizes, interfaces and pathway characteristics were calculated as described elsewhere [37,38]. In Table 1, the connected phase

fraction, is the fraction of each phase that has a connecting pathway to all 6 sides of the data cuboid. In order to obtain additional information on the quality of the phase networks, TPB tortuosity and TPB critical pathway radius were computed. The TPB tortuosity is defined as the ratio between the shortest distance from the TPB site to its source/destination through a specific phase, divided by the Euclidian distance across all phase boundaries. The TPB critical pathway radius is defined as the radius of the largest sphere that can reach a TPB through a particular phase. It is worth noticing that, if a TPB site is connected through all the three phases, the path through Ni, YSZ and Pore network (to reach the TPB) can have a different tortuosity. Both the TPB tortuosity and the TPB critical pathway radius is computed for each TPB site (a certain voxel) and each phase. The detailed procedure to calculate the TPB tortuosity and TPB critical pathway radius distributions are reported in [39]. All the algorithms for segmentation and data analysis were written in-house using MATLAB®.

3. **Results**

3.1 Microstructural evolution and statistical analysis

Figure 1 visually summarizes the effect of the annealing on the microstructure where the same slice of the spatially registered volumes is presented.

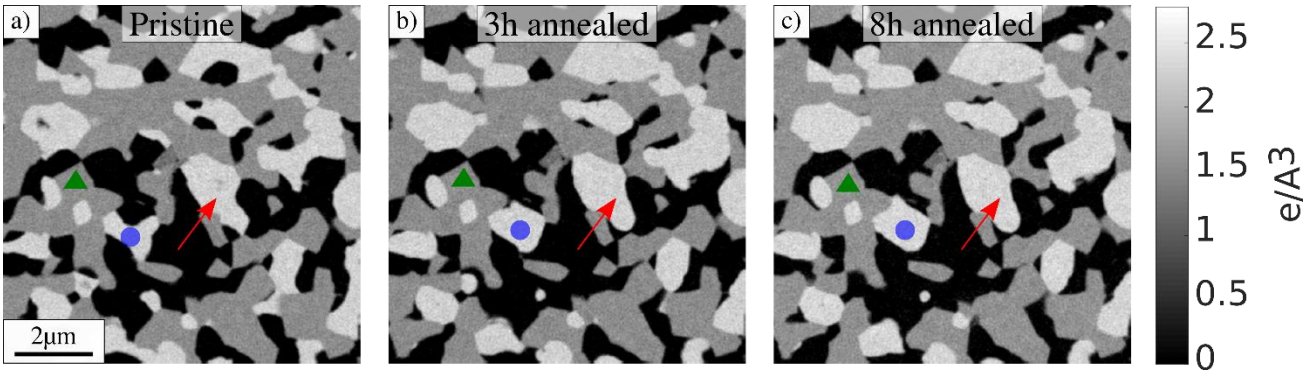

Figure 1. Two dimensional slices from a spatially registered sub-dataset at identical locations in the electrode in the pristine (a), annealed for 3 hours (b) and for 8 hours (c) states. Three different grey levels are present: black (pore), grey (YSZ) and white (nickel). The green triangular markers indicate the same feature of the electrode to show the alignment of the datasets. The red arrows and blue circles indicate example locations where the effect of coarsening is visible. The colour scale indicates the electron density.

The original microstructure in its pristine state (Figure 1a) is directly compared with 3 hours (Figure 1b) and 8 hours (Figure 1c) of cumulative exposure at 850 °C. Taking the value of the electron density corresponding to the peak of the histogram corresponding to the nickel phase, a mass density of 9.026 g/cm^3 is obtained. This value is in good agreement with the nickel theoretical density equal to 8.908 g/cm^3.

From Figure 1, for the given experimental conditions, the three following qualitative observations can be made:

i) The YSZ network does not change detectably.

ii) After annealing, the nickel network appears to coarsen and sharp edges evolve towards more rounded surfaces (red arrows in Figure 1).

iii) From 3 hours to 8 hours of treatment, the changes in the microstructure are less pronounced if compared to the microstructure evolution observed during the first 3 hours of treatment. As an example, the shape of the particle indicated by the blue circles evolves considerably from the pristine to the 3 hours annealed state. However, only a few changes can be observed from the 3 to the 8 hours annealed states.

For the microstructure statistical analysis, a sub-set of 9x9x6 µm^3 in the electrode active layer was extracted from each of the spatially registered datasets (see Figure S2 in the supplementary material). Microstructure parameters of the electrode in different states are reported in **Table 1**.

	Pristine	**3h annealed**	**8h annealed**
Pore/YSZ interface [µm^2/ µm^3]	1.18	1.30	1.30
Pore/Ni interface [µm^2/ µm^3]	0.64	0.57	0.54
Ni/YSZ interface [µm^2/ µm^3]	0.97	0.83	0.84
Pore interface [µm^2/ µm^3]	1.82	1.87	1.84
YSZ interface [µm^2/ µm^3]	2.15	2.13	2.14
Ni interface [µm^2/ µm^3]	1.61	1.40	1.37
Total TPB density [µm/ µm^3]	2.70	2.43	2.35
Percolating TPB density[µm/ µm^3]	2.04	2.02	1.92

Nickel phase fraction [-]	0.28	0.28	0.28
YSZ phase fraction [-]	0.43	0.42	0.43
Pore phase fraction [-]	0.28	0.29	0.29
Connected Nickel fraction [-]	0.96	0.95	0.94
Connected YSZ fraction [-]	0.99	0.99	0.99
Connected Pore fraction [-]	0.94	0.99	0.99

Table 1. Microstructure parameters of the electrode in the pristine, 3 hours and 8 hours annealed states

This comparison is made on the same volume of the three datasets, making the analysis less prone to statistical uncertainties due to representative volume size. However, errors may arise from non-reproducibility in the segmentation of the three different datasets. In this case, we can estimate the segmentation error analyzing the overall YSZ interface areas reported in Table 1. Since the YSZ is expected to remain unchanged during the thermal treatment, we can calculate that our segmentation is accurate to within a maximum error of ~1 %.

From the calculated nickel and YSZ fractions, we can compute that the Ni-YSZ volumetric ratio agrees with the fabrication parameters within 2%.

Table 1 shows that from the pristine to the 8 hour annealed electrode, the changes in the YSZ and Pore surface areas are negligible (in the range of the segmentation error), while the total Ni interface area decreases from 1.61 to 1.37 $\mu m^2/\mu m^3$. Furthermore, the Ni-YSZ interface area decreases 13.4% from the initial value, while the Pore-YSZ interface increases by 9.2 %. Interestingly, while the total TPB density is reduced from 2.70 to 2.35 $\mu m/\mu m^3$, the percolating TPB density decreases only from 2.04 to 1.92 $\mu m^2/\mu m^3$ after 8 hours of annealing.

Figure 2a shows the cumulative particle size distribution (PSD) of all three phases of the electrode, in the pristine state, after 3 hours and 8 hours of annealing. From 2a, the YSZ continuous particle size distribution (c-PSD) in the different states is observed to be almost identical. The pore c-PSD presents a slightly higher fraction of pore regions with smaller radii after annealing. A greater difference is observed in the c-PSD of nickel, which presents a significantly coarser microstructure. In line with the observations from Figure 1, the particle size distribution shifts considerably towards larger structures from the pristine to the 3 hour annealed state, while only evolving slightly after 8 hours of treatment. However, the data show that the trend is preserved and the nickel coarsening continues even if at a slower rate.

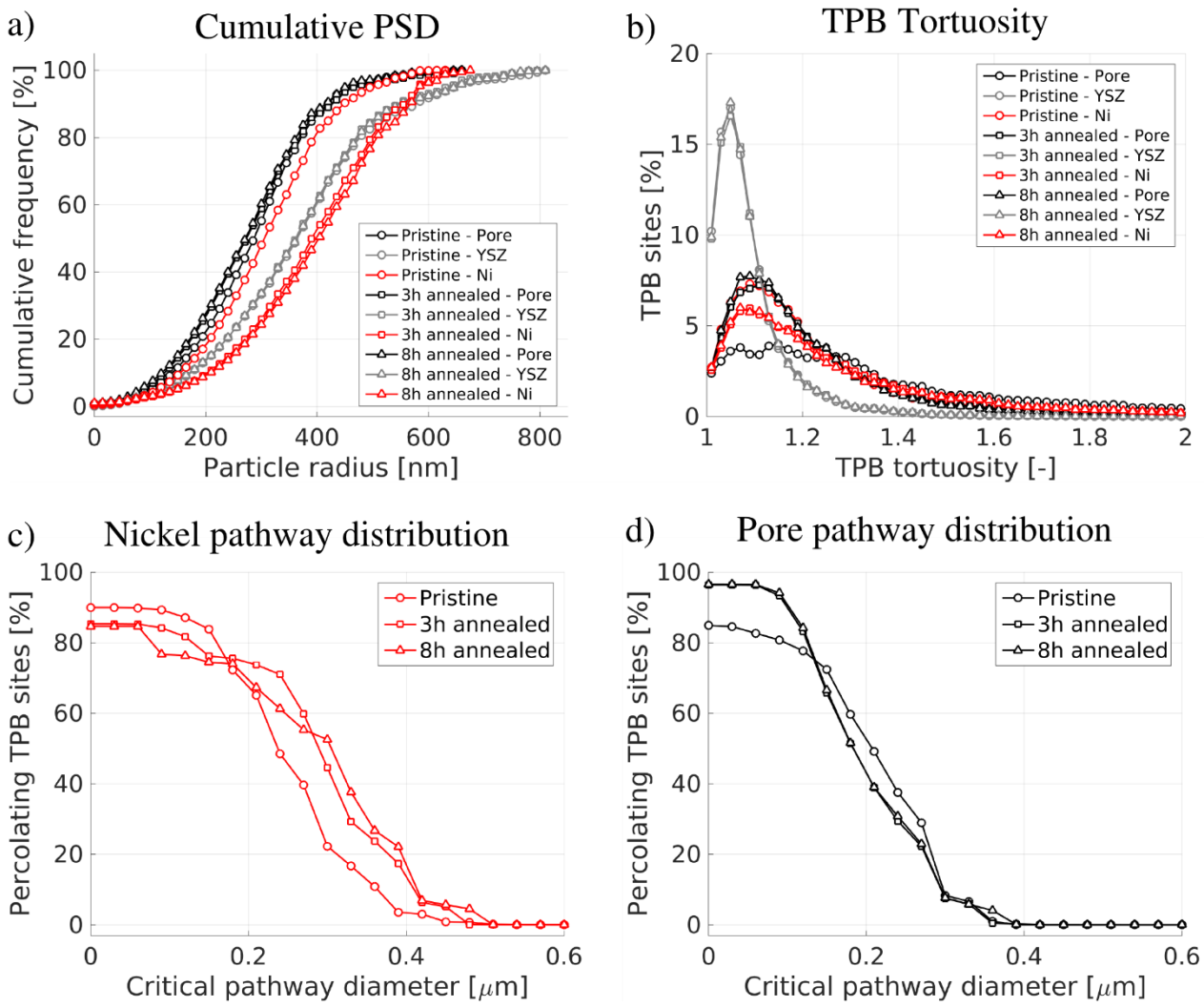

Figure 2. Cumulative PSDs (a), TPB tortuosity (b) and TPB critical pathway diameter (c, d) for the electrode in the pristine, 3 hours and 8 hours annealed state. In (a) and (b) all three phases are included. In (c) and (d) only the critical pathways distributions for nickel and pore respectively are shown.

Figure 2b, shows the TPB tortuosity evolution for all three phases. The distribution for the YSZ phase is almost identical for all the three datasets, supporting that the YSZ network does not evolve significantly. The pore network has significantly fewer TPB sites with low (<1.2) tortuosity values in the pristine state compared to the annealed states. A different behavior is observed for the nickel network, which presents a drop in the fraction of direct pathways in the 3 and 8 hours annealed states. As for the PSD, the most significant change in TPB tortuosity is observed between the pristine and 3 hour annealed electrode, whereas an additional 5 hours of annealing results in negligible change.

Figure 2c and 2d show the evolution of the critical pathway thickness for the electrode in the different states for nickel (2c) and pores (2d). The curves for the static YSZ network are omitted. Figure 2c shows that, while more TPBs are connected through the pristine nickel network, the distribution of critical pathway radii drops to zero more rapidly. Therefore, in the annealed states, the TPBs are connected through pathways with larger diameter bottlenecks in the nickel phase. The pore phase shows the opposite trend (figure 2d). The pore networks in the annealed states connect a larger fraction of TPBs while they present smaller critical pathway radii. As observed for the PSD and TPB tortuosity, also the critical pathway analysis confirms that most of the microstructure evolution observed in this study occurs after only 3 hours of treatment.

4. **Discussion**

4.1 **Nickel coarsening in a SOCs electrode**

As summarized in [40,41], two main mechanisms for nickel coarsening have been proposed in the literature:

i) Evaporation-deposition of Ni volatile compounds.

ii) Ni-Ni inter-diffusion which can occur either on particle surfaces (surface diffusion) or through the bulk of the network (bulk diffusion) [7,17]. However at SOC typical operating temperature, the Ni lattice (bulk) diffusion coefficient is estimated to be in the order of 10^{-16} m^2s^{-1} while the surface diffusion coefficient is in the order of 10^{-11} m^2s^{-1} [21,42]. Therefore, one can assume that the main transport mechanism is the surface diffusion.

The isolated nickel particles present a convenient system to assess the nature of nickel coarsening. Being disconnected from the main Ni network, changes in volume can only be due to nickel transport to other phases, as in the case of nickel evaporation/deposition (through pores).

Figure 3 shows a 3D rendering of the isolated nickel particles in the same volume used in the statistical analysis from the pristine (a) and after 3 hours of treatment (b) datasets. Since further annealing only produces very few new isolated particles after 8 hours of annealing, to simplify the analysis, only the first two states of the electrode are shown (refer to figure S3 in the supplementary materials for the entire study).

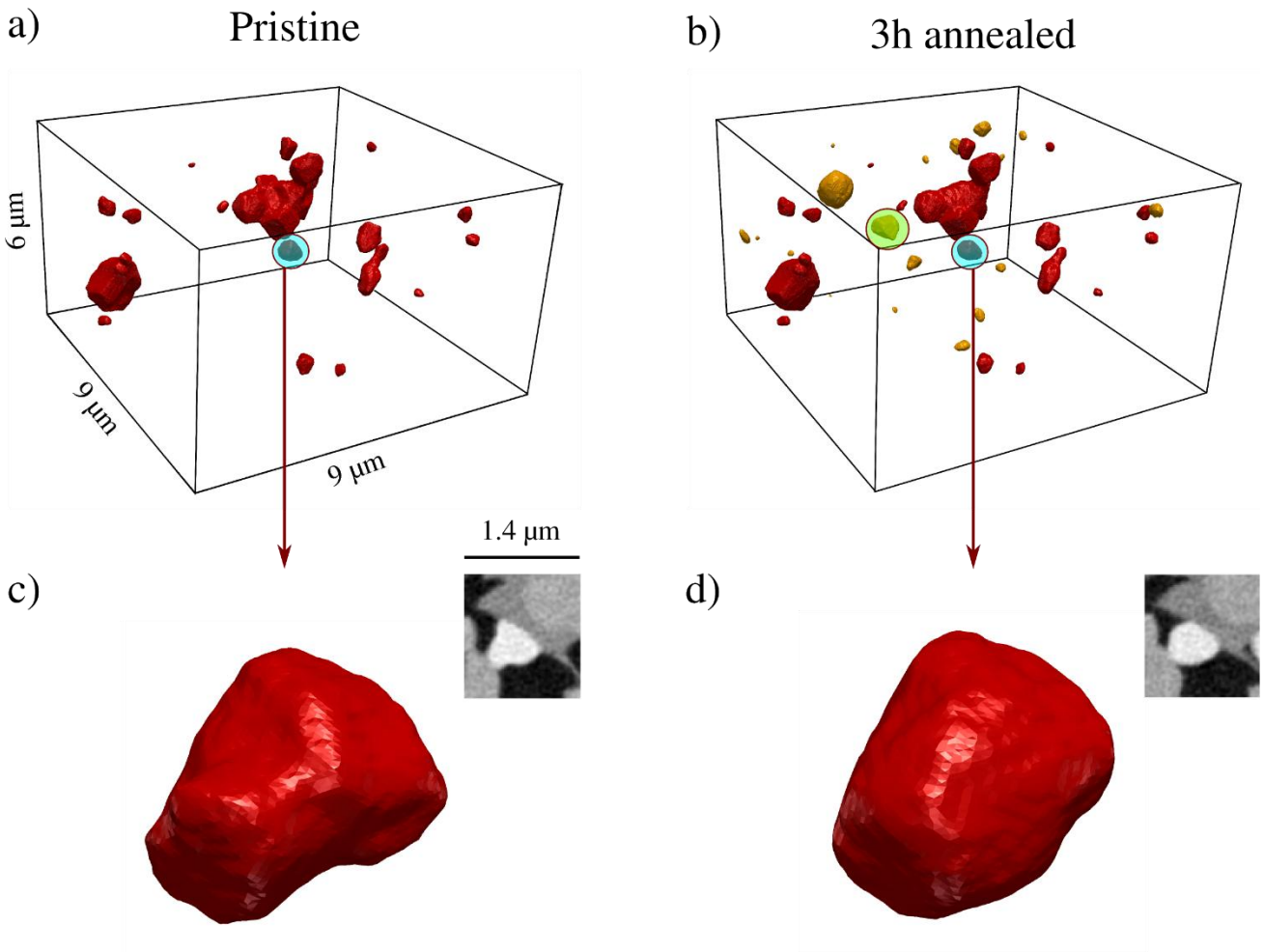

Figure 3. Evolution of isolated nickel particles in the pristine state (a) and after 3 hours of annealing (b). In (b), the orange particles are the newly formed isolated particles after annealing. (c) Magnified view of the highlighted particle in (a). (d) Magnified view of the same particle after annealing. In the insets, the corresponding mid two-dimensional slice from a 1.4x1.4x1.4 µm sub-volume containg the particle is shown. The particle highlighted by the green circle is studied in Figure 4.

Analyzing all the isolated particles in the datasets, the volume of Ni in the different states remains constant within an error of 0.2% and can be attributed to the limits of segmentation accuracy. However, significant morphological evolution is observed from the pristine to the 3 hour annealed state. Thus, we can conclude that at the time scale and conditions of this experiment (850°C in dry hydrogen), the leading phenomenon for the nickel coarsening is the Ni-Ni surface diffusion. Such results are in agreement with the fact that the saturated partial pressure of Ni is negligible at this temperature [43].

As an example, Figure 3c and 3d show the evolution of one isolated nickel particle. The particle in the pristine state presents regions with high curvature, which have higher chemical potential than regions with lower curvature (Gibbs-Thomson effect[7]). Thus, Ni atoms will diffuse from high curvature regions towards regions with lower chemical potentials minimizing the system free energy. This mechanism leads to the nickel particles morphological change observed in Figure 1 and Figure 3d where sharp edges are eliminated in favor of more rounded surfaces. The minimization of curvature and the creation of smoother interfaces has been observed in all the isolated particles shown in Figure 3a and 3b.

4.2 **Effect of the nickel coarsening on the nickel and pore connectivity**

Phase connectivity is a requirement for a working electrode. The electrochemical reaction at the triple phase boundaries can only occur if the phase networks can provide a suitable pathway for electrons (nickel), ions (YSZ) and gas species (pore). The loss of Ni-Ni connections after cell operation has been observed in many previous works and has been reported as one of the main causes of cell degradation [44–46]. Referring to Figure 3, the following observation can be made:

i) The isolated particles in the pristine state remain disconnected in the 3 hours annealed electrode (red particles in Figure 3a and 3b).

ii) Newly formed isolated nickel particles are observed after 3 hours of annealing.

The loss of nickel connectivity plays a role in the microstructural change observed in the statistical analysis. Comparing the pristine and the 3 hour annealed electrode, Figure 2c shows that a smaller fraction of TPBs are percolated in the 3 hour annealed nickel network (percolating TPB sites at zero critical radius). Loss of nickel connectivity can also explain the difference in the pore network. As a consequence of the nickel evolution, new pore channels are created increasing the overall pore connectivity. With the formation of new channels, new pathways are opened resulting in a bigger fraction of TPBs percolated through shorter pathways leading to a decrease of pore TPBs tortuosity (Figure 2b).

To investigate the causes of the nickel connectivity loss, the newly disconnected particles in the 3 hour annealed microstructure are studied in terms of their original connection (in the pristine state) to the rest of the network.

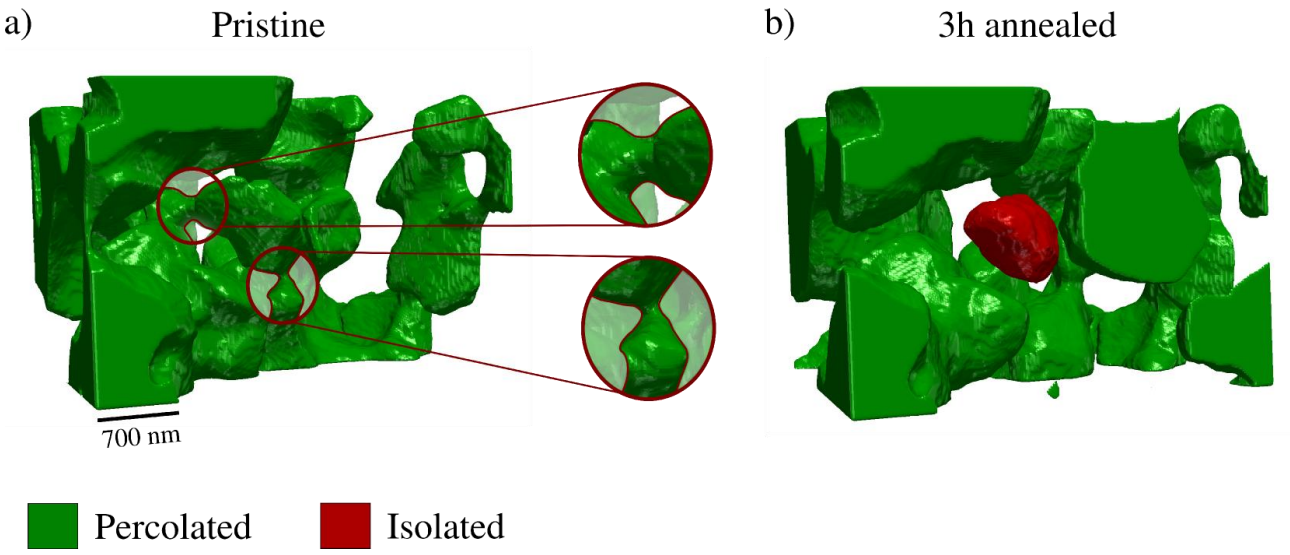

Figure 4. Zoom in on the surrounding nickel network of the particle highlighted by the green circle in Figure 3. (a) Surrounding nickel network of the red particle in (b) in the pristine state. (b) The same region in the 3 hours annealed microstructure.

17 newly formed isolated particles were detected after 3 hours of annealing. From 3 to 8 hours of thermal treatment, only 2 new disconnected particles were observed.

As an example, Figure 4 shows a magnified view of the surrounding region of the particle highlighted in figure 3b (green circle). In figure 4b, the isolated particle is colored in red while the rest of the network is colored in green, as it remains connected outside the volume of interest shown in figure 4. For the sake of clarity, the YSZ network that supports the isolated Ni particle is not shown.

In the pristine state, the isolated particle in figure 4b was connected through only two narrow channels often referred to as "*bottlenecks"* (magnified regions in figure 4a). The disappearance of these bottlenecks leads to the formation of two separated interfaces causing the Ni-Ni disconnection. We speculate that this phenomenon is caused by the high Ni/YSZ interfacial energy. Following this assumption, the system is more energetically favored to create new Ni/Pore interfaces. In the region of small bottlenecks, this results in nickel disconnection.

This phenomenon has been observed in all the 17 particles. The diameters of the bottlenecks were manually measured from 2D slices. From this analysis, we observed that all the new isolated particles were connected to the Ni network through narrow channels with diameters ranging from 50 nm to 250 nm.

The disappearance of the small bottlenecks represents one of the major effects of the nickel coarsening at this time scale. It is worth mentioning that, such phenomenon occurs in the entire nickel network and does not

always lead to loss in nickel percolation. Even if a small bottleneck disappears, two or more regions can still be connected through other available pathways. However, Ni/Ni disconnections that do not result in isolation, reduce the number of alternative pathways, thus the increase in TPB tortuosity observed in Figure 2b.

The disappearance of bottlenecks is also in line with the nickel critical pathway radius distribution presented in Figure 2c. Particles which are connected only through small bottlenecks will become disconnected leading to the decrease in TPB percolation, while the disappearance of narrow channels in the connected network leads to the shift towards bigger critical radii observed in Figure 2c.

4.3 **Effect of the nickel coarsening on the triple phase boundaries**

Table 1 shows that after 3 hours of annealing, the total TPB density decreases considerably (from 2.70 to 2.43 µm/ µm^3) from its original value. During coarsening, in some regions of the electrode, nickel tends to become detached from the YSZ network (nickel *de-wetting*) resulting in the decrease of Ni/YSZ interface area reported in Table 1. Therefore, the TPBs defined by the outline of the Ni/YSZ interfaces shrink in the annealed states.

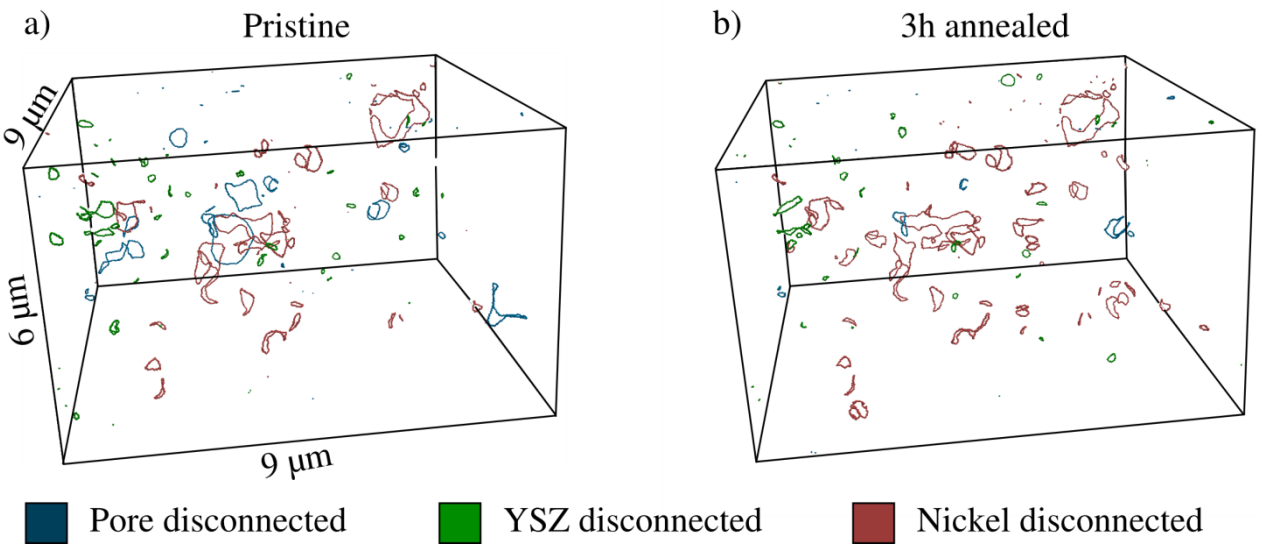

Figure 5. Isolated TPBs in the pristine (a) and 3 hours annealed state. In (a) and (b), the pore, YSZ and nickel disconnected TPBs are colored in blue, green and red respectively.

This phenomenon can be observed in the behavior of the region of the nickel network indicated by the red arrows and the blue circles in Figure 1. The bottom tip of the particles, originally connected to the YSZ,

become detached in the annealed states (more instances of the same phenomenon are reported in Figure S4 in the supplementary materials). This observation is in line with previous reports [8,9], where the contact angle between nickel and YSZ has been estimated to be in between 110° and 120°, testifying low wettability between the two materials.

Based on the decrease of total TPB density and the loss of nickel connectivity, it is reasonable to expect a considerable reduction of percolated TPB density. However, Table 1 shows only a limited decrease in percolated TPB density, from 2.04 to 1.92 after 8 hours of annealing. In order to explain this observation, the isolated TPB sites are identified and their evolution is tracked in the different states of the electrode. Figure 5 shows the isolated TPBs in the pristine (Figure 5a) and the 3 hours annealed state (Figure 5b). The reader can refer to Figure S5 in the supplementary material for the entire study. A TPB site is not connected through a particular phase if it cannot be reached starting from any side of the volume. Comparing Figure 5a and 5b, one can notice that accordingly to the formation of new isolated nickel particles (see Figure 3b), new nickel disconnected TPBs appear in the annealed microstructure. Quantitatively, this is reported in Figure 2c where there is a drop in Ni TPB percolation from 90 to 85%. Contrarily, the TPBs isolated through the pores almost disappear in the 3h treated electrode. Due to the improved connectivity of the pore network, previously isolated TPBs become percolated. Therefore, even though the total TPB density decreases considerably, this effect is counter balanced by the opening of new available pore pathways for early stage annealing.

4.4 **Future perspective**

In the previous sections we demonstrated that, for a Ni-YSZ microstructure reduced for 1 hour at 850 °C, most of the morphological changes occur during the first three hours of treatment at 850 °C. These results are in agreement with *Kennouche et al.* who observed a similar behavior for a Ni-YSZ microstructure treated at 900°C [15]. Instabilities of SOC microstructures, in the first hours of treatment, has been also observed in Ni-YSZ nano-structured electrodes[47]. During the past years, it has been reported that different reduction conditions leads to different cell microstructures[48]. It is also shown that, the morphology of the initial microstructure (after reduction), influences the long-term nickel coarsening[13]. However, while most of the previous studies focus on the evolution of microstructures after hundreds of hours of treatment, more efforts

are needed to characterize the early stages of nickel coarsening. In this regard, other important factors such as humidity must be investigated in more detail in terms of their influence on the initial coarsening. The initial evolution of a similar Ni-YSZ microstructure (from the same electrode material) treated in humidified hydrogen will be the topic of a future publication.

Lastly, the datasets acquired in this experiment provide the ground truth for future and more accurate nickel coarsening models. For example, the evolution of isolated particles offer an ideal system to be compared with coarsening simulations. As the nickel particle is entirely enclosed in the volume of interest, simulations will be less dependent on the conditions applied to the volume boundaries. Furthermore, material parameters (difficult to obtain experimentally) such as Ni surface energy, Ni mobility and Ni-YSZ surface energy can be estimated by matching simulation results with experimental data using an iterative approach [49]. Models with improved accuracy developed using the presented datasets (DOI:10.5281/zenodo.1040274) can be used to virtually assess the long-term performance of a particular microstructure and, ultimately, can represent a highly valuable design tool for future rationally-designed microstructure. Nickel coarsening simulations based on the phase-field model on the presented datasets will be the focus of a future paper.

5 **Conclusions**

The 3D microstructural evolution of a solid oxide cell electrode was observed while treated at high temperature in dry hydrogen using PXCT. The sample was first analyzed in the pristine state and subsequently after 3 and 8 hours of annealing. The high spatial resolution and data quality given by PXCT, allowed the detailed observation of changes in the microstructure occurring during the initial nickel coarsening.

The statistical analysis, revealed that the nickel coarsening causes loss in nickel connectivity, total Ni-Pore interface area, Ni-YSZ interface area and total TPB density. Furthermore, most of the morphological changes are observed during the first 3 hours of treatment.

The analysis of the evolution of isolated nickel particles shows that the nickel coarsening is mainly due to nickel surface diffusion. Therefore, phenomena such as nickel evaporation-condensation can be excluded in the conditions of this experiment.

The nickel coarsening causes the disconnection of narrow nickel bottlenecks which results in the formation of new isolated nickel particles. Furthermore, new pore channels are created leading to improved connectivity of the pore network.

Finally, the study of the evolution of isolated TPBs shows that, the newly created pore channels after annealing results in the activation of many previously non-active TPBs. This phenomenon counterbalances the overall decrease of total TPB density due to the nickel particles coalescence.

Acknowledgements

The authors would like to thank John Johnson for help in designing and building the sample environment, Ebtisam Abdellahi for the challenging sample preparation and Xavier Donath for his technical support at the cSAXS beamline. The authors also thank colleagues at DTU Energy, especially Martina Trini for her valuable help in the data analysis. Financial support from "the allianCe for ImagiNg of Energy MAterials", DSF-grant no. 1305-00032B via "The Danish Council for Strategic Research" is gratefully acknowledged. E. H. R.T is supported by the Swiss National Science Foundation (SNSF) grant number 200021_152554 and SNSF 200020_169623. Travel support for the synchrotron experiment through the DANSCATT grant from the Danish Council for Independent Research is gratefully acknowledged.

References

[1] B. Shri Prakash, S. Senthil Kumar, S. T. Aruna, *Renew. Sustain. Energy Rev.* **2014**, *36*, 149.
[2] S. P. Jiang, S. H. Chan, *J. Mater. Sci.* **2004**, *39*, 4405.
[3] R. J. Kee, H. Zhu, A. M. Sukeshini, G. S. Jackson, *Combust. Sci. Technol.* **2008**, *180*, 1207.
[4] C. Graves, S. D. Ebbesen, S. H. Jensen, S. B. Simonsen, M. B. Mogensen, *Nat. Mater.* **2015**, *14*, 239.
[5] A. Ioselevich, A. A. Kornyshev, W. Lehnert, *J. Electrochem. Soc.* **1997**, *144*, 3010.
[6] S. P. Jiang, *J. Mater. Sci.* **2003**, *38*, 3775.
[7] H.-Y. Chen, H.-C. Yu, J. Scott Cronin, J. R. Wilson, S. A. Barnett, K. Thornton, *J. Power Sources* **2011**, *196*, 1333.
[8] P. Nikolopoulos, D. Sotiropoulou, *J. Mater. Sci. Lett.* **1987**, *6*, 1429.
[9] A. Tsoga, A. Naoumidis, P. Nikolopoulos, *Acta Mater.* **1996**, *44*, 3679.
[10] R. R. Mosbæk, J. Hjelm, R. Barfod, J. Høgh, P. V. Hendriksen, *Fuel Cells* **2013**, *13*, 605.
[11] Z. Jiao, N. Shikazono, N. Kasagi, *J. Electrochem. Soc.* **2012**, *159*, B285.
[12] J.-H. Lee, H. Moon, H.-W. Lee, J. Kim, J.-D. Kim, K.-H. Yoon, *Solid State Ion.* **2002**, *148*, 15.
[13] Z. Jiao, N. Shikazono, *J. Electrochem. Soc.* **2015**, *162*, F571.
[14] J. R. Wilson, J. S. Cronin, S. A. Barnett, *Scr. Mater.* **2011**, *65*, 67.

[15] D. Kennouche, Y. K. Chen-Wiegart, J. S. Cronin, J. Wang, S. A. Barnett, *J. Electrochem. Soc.* **2013**, *160*, F1293.
[16] G. J. Nelson, K. N. Grew, J. R. Izzo Jr., J. J. Lombardo, W. M. Harris, A. Faes, A. Hessler-Wyser, J. Van herle, S. Wang, Y. S. Chu, A. V. Virkar, W. K. S. Chiu, *Acta Mater.* **2012**, *60*, 3491.
[17] R. Vaßen, D. Simwonis, D. Stöver, *J. Mater. Sci.* **2001**, *36*, 147.
[18] X. Wang, A. Atkinson, *J. Electrochem. Soc.* **2014**, *161*, F605.
[19] T. Abdullah, L. Liu, *ECS Trans.* **2015**, *66*, 207.
[20] Y. Lei, T.-L. Cheng, Y.-H. Wen, *J. Power Sources* **2017**, *345*, 275.
[21] R. Davis, F. Abdeljawad, J. Lillibridge, M. Haataja, *Acta Mater.* **2014**, *78*, 271.
[22] Z. Jiao, N. Shikazono, *J. Electrochem. Soc.* **2014**, *161*, F577.
[23] D. Kennouche, Y. K. Chen-Wiegart, K. J. Yakal-Kremski, J. Wang, J. W. Gibbs, P. W. Voorhees, S. A. Barnett, *Acta Mater.* **2016**, *103*, 204.
[24] M. Holler, A. Diaz, M. Guizar-Sicairos, P. Karvinen, E. Färm, E. Härkönen, M. Ritala, A. Menzel, J. Raabe, O. Bunk, *Sci. Rep.* **2014**, *4*.
[25] S. De Angelis, P. S. Jørgensen, V. Esposito, E. H. R. Tsai, M. Holler, K. Kreka, E. Abdellahi, J. R. Bowen, *J. Power Sources* **2017**, *360*, 520.
[26] M. Dierolf, A. Menzel, P. Thibault, P. Schneider, C. M. Kewish, R. Wepf, O. Bunk, F. Pfeiffer, *Nature* **2010**, *467*, 436.
[27] J. J. Lombardo, R. A. Ristau, W. M. Harris, W. K. S. Chiu, *J. Synchrotron Radiat.* **2012**, *19*, 789.
[28] P. R. Shearing, R. S. Bradley, J. Gelb, F. Tariq, P. J. Withers, N. P. Brandon, *Solid State Ion.* **2012**, *216*, 69.
[29] S. L. Ebbehøj, T. Ramos, M. Mogensen, *ECS Trans.* **2012**, *45*, 363.
[30] M. Holler, J. Raabe, A. Diaz, M. Guizar-Sicairos, C. Quitmann, A. Menzel, O. Bunk, *Rev. Sci. Instrum.* **2012**, *83*, 073703.
[31] X. Huang, H. Yan, R. Harder, Y. Hwu, I. K. Robinson, Y. S. Chu, *Opt. Express* **2014**, *22*, 12634.
[32] B. Henrich, A. Bergamaschi, C. Broennimann, R. Dinapoli, E. F. Eikenberry, I. Johnson, M. Kobas, P. Kraft, A. Mozzanica, B. Schmitt, *Nucl. Instrum. Methods Phys. Res. Sect. Accel. Spectrometers Detect. Assoc. Equip.* **2009**, *607*, 247.
[33] P. Thibault, M. Dierolf, A. Menzel, O. Bunk, C. David, F. Pfeiffer, *Science* **2008**, *321*, 379.
[34] M. Guizar-Sicairos, J. R. Fienup, *Opt. Express* **2008**, *16*, 7264.
[35] A. Diaz, P. Trtik, M. Guizar-Sicairos, A. Menzel, P. Thibault, O. Bunk, *Phys. Rev. B* **2012**, *85*, 020104.
[36] P. J. Besl, N. D. McKay, 1992; Vol. 1611, pp. 586–606.
[37] B. Münch, L. Holzer, *J. Am. Ceram. Soc.* **2008**, *91*, 4059.
[38] P. S. Jørgensen, K. V. Hansen, R. Larsen, J. R. Bowen, *J. Power Sources* **2010**, *195*, 8168.
[39] P. S. Jørgensen, S. L. Ebbehøj, A. Hauch, *J. Power Sources* **2015**, *279*, 686.
[40] M. S. Khan, S.-B. Lee, R.-H. Song, J.-W. Lee, T.-H. Lim, S.-J. Park, *Ceram. Int.* **2016**, *42*, 35.
[41] H. Yokokawa, H. Tu, B. Iwanschitz, A. Mai, *J. Power Sources* **2008**, *182*, 400.
[42] K. Maier, H. Mehrer, E. Lessmann, W. Schüle, *Phys. Status Solidi B* **1976**, *78*, 689.
[43] A. I. Zaitsev, N. E. Zaitseva, *High Temp.* **2002**, *40*, 197.
[44] A. Hauch, P. S. Jørgensen, K. Brodersen, M. Mogensen, *J. Power Sources* **2011**, *196*, 8931.
[45] M. H. Pihlatie, A. Kaiser, M. Mogensen, M. Chen, *Solid State Ion.* **2011**, *189*, 82.
[46] P. Tanasini, M. Cannarozzo, P. Costamagna, A. Faes, J. Van Herle, A. Hessler-Wyser, C. Comninellis, *Fuel Cells* **2009**, *9*, 740.
[47] A. Bertei, E. Ruiz-Trejo, K. Kareh, V. Yufit, X. Wang, F. Tariq, N. P. Brandon, *Nano Energy* **2017**, *38*, 526.
[48] M. Andrzejczuk, O. Vasylyev, I. Brodnikovskyi, V. Podhurska, B. Vasyliv, O. Ostash, M. Lewandowska, K. J. Kurzydłowski, *Mater. Charact.* **2014**, *87*, 159.
[49] J. Zhang, S. O. Poulsen, J. W. Gibbs, P. W. Voorhees, H. F. Poulsen, *Acta Mater.* **2017**, *129*, 229.